IOP Publishing Journal of Physics: Condensed Matter

J. Phys.: Condens. Matter **29** (2017) 504005 (15pp) https://doi.org/10.1088/1361-648X/aa9960

Lanthanide stannate pyrochlores ($Ln_2Sn_2O_7$; Ln = Nd, Gd, Er) at high pressure

Katlyn M Turner, Cameron L Tracy, Wendy L Mao and Rodney C Ewing

Department of Geological Sciences, Stanford University, 359 Green Earth Sciences Building,
367 Panama Street, Stanford, CA 94305-2115, United States of America

E-mail: katlynmt@stanford.edu

Received 24 August 2017, revised 6 November 2017
Accepted for publication 9 November 2017
Published 27 November 2017

Abstract

Lanthanide stannate pyrochlores ($Ln_2Sn_2O_7$; Ln = Nd, Gd, and Er) were investigated *in situ* to 50 GPa in order to determine their structural response to compression and compare their response to that of lanthanide titanate, zirconate, and hafnate pyrochlores. The cation radius ratio of A^{3+}/B^{4+} in pyrochlore oxides ($A_2B_2O_7$) is thought to be the dominant feature that influences their response on compression. The ionic radius of Sn^{4+} is intermediate to that of Ti^{4+}, Zr^{4+}, and Hf^{4+}, but the ⟨Sn–O⟩ bond in stannate pyrochlore is more covalent than the ⟨B–O⟩ bonds in titanates, zirconate, and hafnates. In stannates, based on *in situ* Raman spectroscopy, pyrochlore cation and anion sublattices begin to disorder with the onset of compression, first measured at 0.3 GPa. The extent of sublattice disorder versus pressure is greater in stannates with a smaller Ln^{3+} cation. Stannate pyrochlores (*Fd*-3*m*) begin a sluggish transformation to an orthorhombic, cotunnite-like structure at ~28 GPa; similar transitions have been observed in titanate, zirconate, and hafnate pyrochlores at varying pressures (18–40 GPa) with cation radius ratio. The extent of the phase transition versus pressure varies directly with the size of the Ln^{3+} cation. Post-decompression from ~50 GPa, $Er_2Sn_2O_7$ and $Gd_2Sn_2O_7$ adopt a pyrochlore structure, rather than the multi-scale defect-fluorite + weberite-type structure adopted by $Nd_2Sn_2O_7$ that is characteristic of titanate, zirconate, and hafnate pyrochlores under similar conditions. Like pyrochlore titanates, zirconates, and hafnates, the bulk modulus, B_0, of stannates varies linearly and inversely with cation radius ratio from 111 GPa ($Nd_2Sn_2O_7$) to 251 GPa ($Er_2Sn_2O_7$). The trends of bulk moduli in stannates in this study are in excellent agreement with previous experimental studies on stannates and suggest that the size of the Ln^{3+} cation is the primary determining factor of B_0. Additionally, when normalized to r_A/r_B, the bulk moduli of stannates are comparable to those of zirconates and hafnates, which vary from titanates. Our results suggest that the cation radius ratio strongly influences the bulk moduli of stannates, as well as their overall compression response.

Keywords: oxides, high pressure, pyrochlore

S Supplementary material for this article is available online

(Some figures may appear in colour only in the online journal)

Introduction

Pyrochlore-structured oxides, of the general formula $A_2B_2O_7$ where A and B are typically 3+ and 4+ cations, respectively [1, 2], show interesting structural properties and phase transitions in extreme environments, such as high-pressure [3–19], high temperature [29–31], and under ion irradiation [25–27]. Some pyrochlore-structured compounds are resistant to radiation-induced amorphization [25–27], and as such they are of interest as potential waste forms for immobilization of actinides from the nuclear fuel cycle [28].

The pyrochlore structure (*Fd*-3*m*) (figure 1(a)) is an ordered 2 × 2 × 2 superstructure derivative of the fluorite structure (*Fm*-3*m*) [1, 2]. Fluorite-structured compounds,

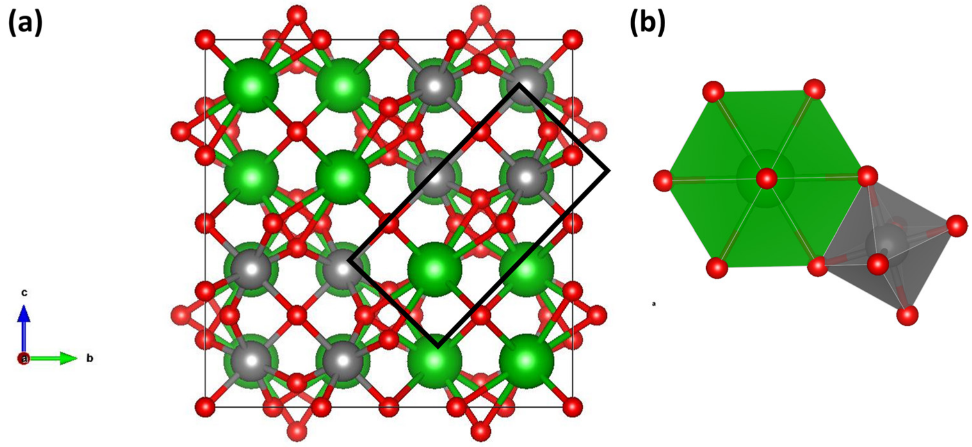

Figure 1. (a) pyrochlore $A_2B_2O_7$ unit cell showing 8-coordinated A (green), 6-coordinated B (grey), and 4-coordinated O (red). (b) Close-up of boxed section in (A) of an edge-shared AO_8 and BO_6 polyhedra in pyrochlore.

with a formula AX_2 where A is a metal and X is typically O or F, exhibit a single cubic-coordinated cation site and a single tetrahedrally-coordinated anion site [1, 2]. In contrast, $A_2B_2X_7$ pyrochlore compounds (*Fd*-3*m*) exhibit two cation sites hosting different cationic species [1, 2]. The stability of this structure is generally determined by the relative sizes of these cations. For example, pyrochlore-structured titanates and zirconates are stable when the cation radius ratio is in the range $1.46 < r_A/r_B < 1.78$ [1, 2]. Titanate and zirconate compositions with a cation radius ratio outside of this range typically form lower symmetry phases [1, 2].

When the origin of the unit-cell is defined at the A-site, relatively large A^{3+} cations (figure 1(a), green) occupy the 16*c* site, where they are coordinated by eight anions in a scalenohedral arrangement (figure 1(b)) [1, 2]. Smaller B^{4+} cations (figure 1(a), grey) occupy the 16*d* site and are coordinated by six anions in a distorted octahedral arrangement (figure 1(b)) [1, 2]. Thus, the cation-sublattice is face-centered cubic with the A- and B-cations alternating along the $\langle 1\,1\,0\rangle$ directions. The anion sublattice in pyrochlore (figure 1(a), red) approximates a simple cubic arrangement, yet the anions are displaced slightly from the ideal simple cubic positions and 1/8 of these positions are vacant to provide charge neutrality in the presence of trivalent cations. All anions are tetrahedrally coordinated by either two A-site cations and two B-site cations (48*f* site), or by four A-cations (8*a* site), while the systematically vacant 8*b* site is tetrahedrally coordinated by four B-cations [1, 2].

Recently, the structural response of pyrochlore-type materials to high pressure, high temperature, and ion irradiation has seen a renewed interest due to the discovery that the disordering processes of pyrochlore in these extreme environments lead to the formation of multi-scale structures [14, 25, 27]. The energetics of defect-formation mechanisms in pyrochlore-type materials [21–24] cause certain compositions to undergo disordering phase transitions rather than to become amorphous in extreme environments [3–18, 25–27, 29–31]. The cation- and anion-sublattices in pyrochlore-structured materials have different defect-formation mechanisms [21–24]. Cations disorder primarily via anti-site defects, wherein A- and B-site cations swap sites [21–24]. Pyrochlore compositions with a low radius ratio, r_A/r_B, are generally more susceptible to cationic disorder, since the sizes of the A and B species are similar [21–24]. For example, under identical synthesis conditions, zirconates ($A_2Zr_2O_7$) have intrinsically more cation disorder as measured by 16*c* and 16*d* site occupancies via x-ray diffraction (XRD) than titanates ($A_2Ti_2O_7$) with the same A-site cation [15, 45, 46]. The anion-sublattice disorders primarily via the formation of Frenkel defect pairs [15–18, 52–54]. Because the pyrochlore structure contains a high number of constitutional anion vacancies, the anion-sublattice has a low activation energy for defect-formation relative to the cation-sublattice [21–24, 52–54]. Additionally, when cationic disorder occurs, anion disordering is even more likely, since cation disorder makes the electronic environment of the 16*c* and 16*d* sites indistinguishable, such that occupation of an initially empty 8*b* site is energetically inexpensive [21–24]. During compression, anion disorder is thought to precede cation disorder due to the ease of 'oxygen-hopping' in pyrochlore [5].

Due to the combination of defect-formation mechanisms in the pyrochlore structure, which allow the structure to incorporate defects on its distinct sublattices without complete loss of this sublattice ordering [21–24], pyrochlore compounds often disorder rather than amorphize at high pressure, high temperature, and under ion irradiation [3–18, 25–27, 29–31]. Some pyrochlore-compositions with a large radius ratio ($r_A/r_B \sim >1.6$)—notably the lanthanide titanates—do amorphize under ion-irradiation and at high pressure [9, 11–13]. However, when defects are formed on the cation and anion sublattices, many pyrochlore compositions, particularly those with a low cation radius ratio, and thus low anti-site formation energies, will merely disorder to a defect-fluorite structure, in which the cations exhibit a solid solution on a single site, and the anions are in a single, 7/8 occupied site with random arrangement of the vacancies [3–7, 9, 10, 13–15, 25–27, 29–31]. The defect-fluorite structure has two distinct length-scales and structural domains that have only recently been discovered [27]. Long-range (>15 Å), disordered $A_2B_2O_7$ compounds are best described as a cubic, defect-rich fluorite structure [27]. This structure is readily observed using conventional synchrotron powder XRD, as well as neutron diffraction [27]. However, at less than 15 Å, the materials are best described as an orthorhombic, weberite-type structure [27]. The weberite-type structural units tessellate in such a way that they coexist with the defect-fluorite structure on different length scales. The average long-range structure as observed by synchrotron powder XRD is defect-fluorite, and the only way to observe the weberite-type structure is by using neutron diffraction and pair distribution function analysis [27] or *in situ* Raman spectroscopy [14, 25]. These techniques are more sensitive to changes in the oxygen coordination environment and ordering than XRD [25, 27]. This multi-scale structure has been observed in pyrochlores that were disordered via compositional doping [27], ion irradiation [25, 27], and possibly at high pressure [14].

The behavior of lanthanide titanate, zirconate, and hafnate pyrochlores in extreme environments are often compared, since Ti, Zr, and Hf are each group four elements that adopt identical valence electron configurations while varying in B^{4+} cation size [3–15, 25–27]. Under compression, hafnate, zirconate, and some titanate pyrochlores transform to an orthorhombic cotunnite-like structure at pressures of at least ~25 GPa [3–15]. During decompression, *in situ* XRD indicates that this cotunnite-like structure typically transforms to either an amorphous or a disordered defect-fluorite phase, depending on composition [3–15]. Lanthanide titanate pyrochlores have the largest radius ratios as compared with zirconates and hafnates and are more prone to amorphization under compression and decompression. Pyrochlore hafnates, zirconates, and titanates that transform to the cotunnite-like structure under pressure typically begin this transformation between 20–30 GPa; it is a sluggish transition that progresses over a range of 15–30 GPa [3–15]. The onset-pressure is sometimes correlated directly with the cation radius-ratio. The onset-pressure of the phase transition is systematically highest in titanates (~40 GPa), and lowest in zirconates (~18 GPa) [15].

The cotunnite-like structure is characterized in *in situ* XRD by a reduced intensity of the strongest pyrochlore Bragg peaks—the (2 2 2) and (4 0 0) maxima—and an appearance of several new peaks. The two most prominent new peaks occur between the (2 2 2) and (4 0 0) pyrochlore diffraction maxima [3–15]. These features are attributed to the cotunnite-like structure [3–15]. The cotunnite-like structure is thought to arise from distortion of the AO_8 scalenohedra and the BO_6 octahedra, and an increase in cation coordination number [5]. The structural details of the cotunnite-like high pressure phase are not well-known. It has been described as 'cotunnite', 'cotunnite-type', 'defect-cotunnite', and 'cotunnite-like' [3–15]. The ideal cotunnite structure has one cation site, which is coordinated by eight anions, similar to the eight-coordinated A-cation site in pyrochlore. When pyrochlore and defect-fluorite structured oxides transform at high pressure, the resulting phase is best described as 'cotunnite-like': it has an overall increase in coordination number of the cations from six and eight in pyrochlore to eight, nine, or ten in the cotunnite-like structure [9]. However, due to the vacancies already present in the pyrochlore structure, the cotunnite-like high pressure phase likely has many anion vacancy defects [9–12]. The cations in the cotunnite-like phase are likely disordered by the formation of anti-site defects onto one cation site [9, 10]. The cation-oxygen bonds in the cotunnite-like structure are lengthened as compared with pyrochlore, due to the increase in coordination number [9]. The pressure-induced transition to the cotunnite-like high pressure phase has been observed in lanthanide zirconate, titanate, and hafnate pyrochlores using *in situ* synchrotron XRD [3–14]. However, due to its coexistence with the pyrochlore phase over a range of pressures—sometimes 15 GPa—and the fact that it is not an ideal cotunnite-type structure, rather a disordered one with intrinsic defects, the structure could not be refined [3–14]. Based on indexing of the peaks in the experimental data, as well as *ab initio* models of the structure of pyrochlore upon compression which predict a transition to a defect-heavy, cotunnite-like structure, the high-pressure structure is described as cotunnite-like [5–10, 12]. Typically, when decompressed from high pressure (50+ GPa) to ambient conditions, the materials will transform into a disordered defect-fluorite structure, sometimes with an amorphous component [3–15]. Although pyrochlore-structured materials of varied compositions undergo similar changes in extreme environments—e.g. disordering, formation of cotunnite-like phases—the specifics of these transformations—e.g. onset pressures or the extent of transition as a function of pressure—vary with composition.

The behavior of lanthanide stannate compounds ($Ln_2Sn_2O_7$) in extreme environments including high pressure is of particular interest due to their deviation from some of the typical compositional trends of the pyrochlore system [25]. For example, all lanthanide stannates adopt pyrochlore structures, despite the fact that those with small lanthanides have cation radius ratios below the typical stability limit of $r_A/r_B = 1.46$ [1, 34–38]. Tin is a group 14 element, but Sn^{4+} has an ionic radius of 0.69 Å, which is comparable to Zr^{4+} (0.71 Å) and Hf^{4+} (0.72 Å). Theoretical calculations show that the degree of covalency of $\langle$Sn–O$\rangle$ bonds in pyrochlore is higher than those of both $\langle$Ti–O$\rangle$ and $\langle$Zr–O$\rangle$ bonds [34–38]. Differences in the electronegativity of Sn (1.8), Zr (1.4), and Ti (1.5) support the classification of $\langle$Sn–O$\rangle$ bonds as covalent, and $\langle$Zr–O$\rangle$ and $\langle$Ti–O$\rangle$ bonds as ionic [48]. Previous work found the oxygen 2p band width in $\langle$Sn–O$\rangle$ to be 7.6 eV, versus ~4 eV for $\langle$Ti–O$\rangle$ and $\langle$Zr–O$\rangle$ [55]. In lanthanide stannate pyrochlores, the unit cell parameter and the 48*f* oxygen positional parameter are primarily a function of the Ln^{3+} ionic radius [35, 58, 59]. A neutron diffraction study of $Ln_2Sn_2O_7$ pyrochlores across the lanthanide series found that the Ln^{3+} ionic radius varies by up to 20%, while the length of the $\langle$Sn–O$\rangle$ bond varies by approximately 1% [58]. The enthalpy of formation of stannate pyrochlores has been shown to increase as a function of Ln^{3+} size [35, 58, 59].

There is debate on whether the bond-type or cation-size mismatch is the dominant structural property in pyrochlore $A_2B_2O_7$ compositions that determines their behavior in extreme environments [25]. For example, computational simulations of $Y_2Ti_2O_7$ and $Y_2Sn_2O_7$ showed nearly identical defect formation energies, despite the large difference in the cationic radius ratio ($r_A/r_B = 1.68$ versus 1.47, respectively) [55]; this similarity was attributed to the covalency of the ⟨Sn–O⟩ bond [55]. Additionally, Ln_2Sn_2O7 stannates were found computationally to have significantly higher disordering energies in eV/formula unit as compared with lanthanide hafnates, zirconates, and titanates [35, 58]; the disordering energy is nearly twice that of identical zirconates [35, 58]. However, prior work on zirconates, titanates, and hafnates attributes compositional variation in behavior in extreme environments to differences in the cation radius ratio [3–15, 25–27, 29–31]. A recent study on the response of stannate pyrochlore compounds to ion irradiation found that their response was consistent with the cation radius-ratio being an important controlling parameter, rather than the covalency of the ⟨Sn–O⟩ bond in the stannates [25].

There are previous experimental studies on the behavior of $Tb_2Sn_2O_7$ [16], $Eu_2Sn_2O_7$ [17, 19], and $La_2Sn_2O_7$ [18] at high pressure, although few to 50 GPa or higher which is often the pressure reached in experiments on titanate, zirconate, and hafnate pyrochlores in order to observe the pressure-induced phase transition to the cotunnite-like structure. A recent study on $Eu_2Sn_2O_7$ examined the material to ~32 GPa and did not find a phase transition to the cotunnite-like phase [17]. The bulk modulus of $Eu_2Sn_2O_7$ in this study was found to be 170 GPa, consistent with experimentally determined bulk modulus estimations for $Gd_2Zr_2O_7$ [17]. An additional study of $Eu_2Sn_2O_7$ to ~45 GPa did not report bulk modulus, but a phase transition to the cotunnite-like high pressure phase was observed to begin at ~34 GPa [3]. Additionally, when quenched from ~45 GPa, $Eu_2Sn_2O_7$ has been observed to revert to a partially ordered pyrochlore structure, rather than amorphizing or transforming to a multi-scale defect-fluorite+ weberite-type structure [3]. A 2007 study on $Tb_2Sn_2O_7$ to ~35 GPa found a bulk modulus of ~200 GPa [16]. A recent study on $La_2Sn_2O_7$ to ~32 GPa reported a bulk modulus of 180 GPa [18]. Additionally, this study reported a phase decomposition to metallic Sn and $La_2Sn_2O_7$ at pressures of ~23 GPa. In a different study, $La_2Hf_2O_7$ was also observed to undergo a phase decomposition at ~18 GPa [19] but instances of phase decompositions in other titanate, zirconate, and hafnate pyrochlores have not been observed.

In addition to the previous experimental work on stannate pyrochlores at high pressure, a recent computational study on the suite of $Ln_2Sn_2O_7$ pyrochlores modeled their behavior and structural parameters upon hydrostatic compression [20]. They found a small variation in bulk modulus of the stannates, from 155 GPa ($La_2Sn_2O_7$) to 175 GPa ($Lu_2Sn_2O_7$). Additionally, the authors modeled the x_{48f} parameter versus hydrostatic pressure, and found that x_{48f} increases with pressure.

Zirconate, titanate, hafnate, and stannate pyrochlore compounds can undergo similar transitions under high pressure and ion irradiation [3–18, 25–27], and the behavior of many of the stannates relative to other pyrochlore compounds has not been explored at high pressure. Additionally, the behavior of stannates under pressure has been recently modeled computationally [20], and found compressibilities and bond-lengths versus pressure that differ from previous experimental studies on stannates, and from previous experimental studies on titanates, zirconates, and hafnates. In order to understand the behavior of lanthanide stannates under pressure, to compare their behavior to that of titanate, zirconate, and hafnate pyrochlores, and to compare their behavior to computationally predicted trends, we have investigated the pressure-induced structural transitions in lanthanide stannate pyrochlores ($Ln_2Sn_2O_7$; Ln = Nd, Gd, Er).

Methods

$Ln_2Sn_2O_7$ (Ln = Nd, Gd, Er) samples were synthesized by solid state methods [25, 38]. SnO_2 and Ln_2O_3 powders were mixed in a stoichiometric (2:1) ratio, and calcined at 1400 °C for 24 h. The structures of the resulting powders were confirmed as pyrochlore via XRD. The samples were then uniaxially compressed at 25 MPa to produce 40 μm-thick wafers (~60% theoretical density), with grain sizes of several micrometers.

For *in situ* analysis at high pressure, small pieces of the $Ln_2Sn_2O_7$ wafers were loaded into symmetric, Mao–Bell type diamond anvil cells (DACs). The diamonds had 300 μm-diameter culets and diamond seats made of cubic boron nitride and tungsten carbide. The samples were contained within cylindrical sample chambers, 100 μm in diameter, drilled into stainless steel gaskets. In addition to the $Ln_2Sn_2O_7$ wafers, each sample chamber included a ruby sphere to measure pressure [40] and a 4:1 by-volume mixture of methanol and ethanol as the pressure-transmitting medium [41, 42].

For *in situ* Raman spectroscopy and XRD measurements, samples were incrementally compressed at 1–3 GPa intervals to a maximum pressure of 50 GPa, and then decompressed in two equal steps of ~25 GPa to ambient pressure. Measurements were performed at each pressure increment. *In situ* Raman spectroscopy measurements were collected in the Extreme Environments Laboratory at Stanford University using a Renishaw RM1000 Raman microscope and a 514.4 nm laser set at a power of 25 mW. Each measurement was collected for 60 s, and Fityk software [43] was used for analysis and peak fitting.

Peak positions, intensities, and profiles were fit for each pressure using a pseudo-Voigt model, and mode Grüneisen parameters were calculated for the Raman-active modes in each composition [44]. The full-width at half maximum (FWHM) of the first F_{2g} mode was measured as a function of pressure, yielding a qualitative measurement of compression-induced disorder in the pyrochlore structure [14].

In situ high-pressure powder XRD measurements were collected at beamline 12.2.2. of the advanced light source (ALS) at Lawrence Berkeley National Laboratory. A MAR345 detector was used, and an x-ray energy of 25 keV ($\lambda = 0.4959$ Å) was used. The size of the beam on the sample was 25 × 25 micrometers; significant texturing effects from crystallite averaging were not observed. Diffraction patterns were collected for 120 s at each pressure point. These data were analyzed and refined using Dioptas [45] and MAUD software [46]. For each pressure point, the pyrochlore unit cell parameter (a), atom site occupancies, and isotropic displacement parameters were

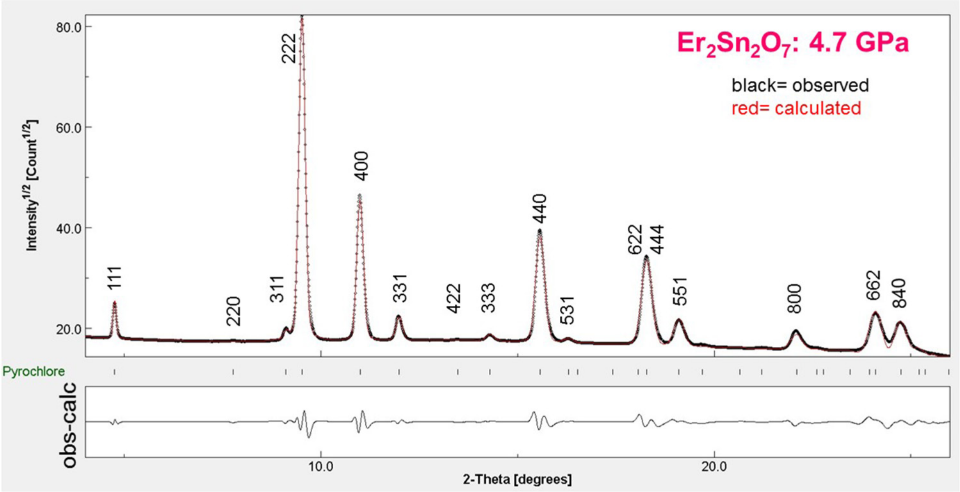

Figure 2. Indexed and refined fit of $Er_2Sn_2O_7$ pyrochlore at 4.7 GPa showing observed pattern (black), calculated fit (red), and difference plot (lower panel).

refined to an Rwp value of no more than 7% (tables S1, S2 and S3). As discussed in the Introduction, the data obtained from the cotunnite-like high pressure phase could not be refined, as in previous studies [3–14], due to the extent of disorder in the phase and the coexistence of the pyrochlore phase and the cotunnite-like phase. Therefore, Rietveld refinement could not be used to quantify the percentage of each phase at high pressure. However, to qualitatively analyze the extent of the phase transition from the low-pressure pyrochlore phase to the high-pressure cotunnite-like phase, the relative intensities of the strongest diffraction maxima from the cotunnite-like phase to the strongest pyrochlore diffraction maxima (2 2 2) were measured as a function of pressure [14]. The compressibility of each composition was determined by fitting the refined pressure-volume data, collected during compression, to a 2nd-order Birch–Murnaghan equation of state [47] using EOSFit7c software [48]. Because of the hydrostatic limit of the pressure medium used, methanol and ethanol in a 4:1 ratio [41, 42], only data from pressure points less than ~12 GPa were used for the 2nd-order Birch Murnaghan equation of state [47] fittings. Errors for the equation of state fits in V_0 and B_0 were propagated from MAUD errors in the unit cell parameter.

Results

In situ XRD

Lanthanide stannates have XRD patterns of the pyrochlore structure (figures 2 and 3). The pyrochlore supercell diffraction maxima from the (1 1 1) and (3 1 1) are clearly present, confirming a pyrochlore-type long range structure, as is expected from the radius ratio of Ln^{3+}/Sn^{4+} (table 1) [1]. The XRD data from each pressure point for each composition were indexed and refined using the Rietveld method. An example characteristic Rietveld-refined XRD pattern showing the observed data, calculated fit, and difference curve from $Er_2Sn_2O_7$ at 4.7 GPa is shown in figure 2. Pyrochlore ordering at low pressure was observed in all samples.

In situ XRD patterns from compressed $Nd_2Sn_2O_7$, $Gd_2Sn_2O_7$, and $Er_2Sn_2O_7$ at selected pressure points are shown in figure 3. A transformation to a high-pressure phase is evident, yet these transformations remain incomplete at the highest pressure measured, as indicated by the presence of peaks corresponding to the initial pyrochlore structure. The peaks corresponding to the high-pressure phase were indexed to the cotunnite-like phase that is commonly observed in pyrochlore hafnates, zirconates, and titanates under pressure [3–15]. The onset of the phase transition for stannates is ~28 GPa for all compositions studied here, higher than the onset pressures reported for hafnates and zirconates, (~15–25 GPa), and lower than that of titanates (~34 GPa) [3–15]. The stannates were decompressed from the maximum pressure achieved (~50 GPa) in two steps of approximately ~25 GPa. Upon decompression, the stannates slowly transform from the cotunnite-like high pressure phase, which is present until decompression to ambient pressure. The XRD patterns of $Gd_2Sn_2O_7$ and $Er_2Sn_2O_7$ (figure 5) indicate that the decompressed material in ambient conditions exhibits both pyrochlore-structured and amorphous or highly disordered phases, as the (1 1 1) diffraction maximum corresponding to the pyrochlore superstructure is still present, yet the intense (2 2 2) peak is superimposed on a broad, diffuse scattering band. Typically, zirconate, titanate, and hafnate pyrochlore compositions compressed to 50 GPa then decompressed to ambient conditions will quench to a disordered defect-fluorite structure, rather than a pyrochlore structure [3–15]. However, a study on $Eu_2Sn_2O_7$ to ~45 GPa also observed the retention of an ordered pyrochlore structure in the quenched phase [3]. $Nd_2Sn_2O_7$ compressed to 50 GPa and quenched to ambient pressure shows an XRD pattern characteristic of a disordered defect-fluorite structure (figure 3). The retention of the pyrochlore structure following decompression from high pressure appears to be unique to $Eu_2Sn_2O_7$ [3], $Gd_2Sn_2O_7$ and $Er_2Sn_2O_7$ stannate pyrochlores.

Each compound begins to transform to the high-pressure cotunnite-like phase at ~28 GPa (±2 GPa). The onset of the

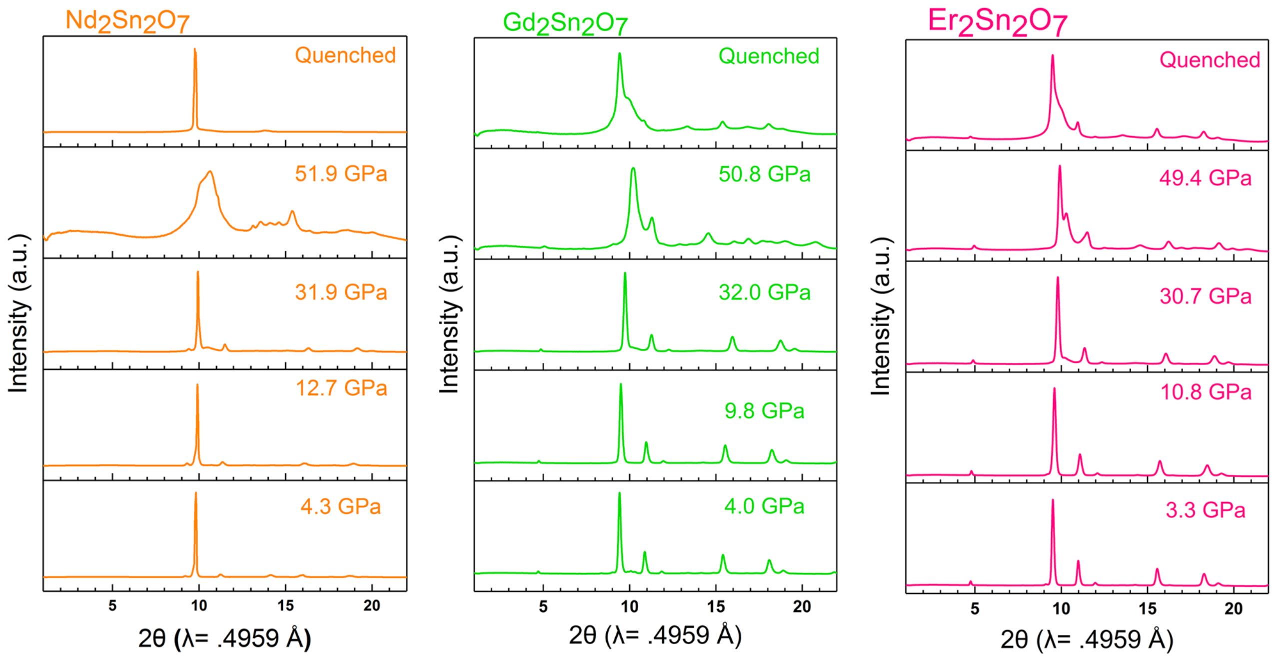

Figure 3. *In situ* XRD of $Nd_2Sn_2O_7$ (L) $Gd_2Sn_2O_7$ (M) and $Er_2Sn_2O_7$ (R) at selected pressure points between 0–50 GPa and quenched to ambient pressure.

Table 1. Ionic radius ratio, Ln^{3+} ionic radii, and ⟨Sn–O⟩ bond lengths [58] of stannate pyrochlore compositions in this study.

Composition	r_A/r_B	r_A (Å)	⟨Sn–O⟩ (Å)
$Nd_2Sn_2O_7$	1.61	1.109	2.06
$Gd_2Sn_2O_7$	1.53	1.053	2.048
$Er_2Sn_2O_7$	1.46	1.004	2.042

transformation was determined by the appearance of peaks between the (2 2 2) and (4 0 0) peaks corresponding to the pyrochlore phase—the strongest of these, if the high-pressure phase were a true cotunnite structure, would correspond to the (1 2 0) cotunnite peak [9]. This compositional uniformity contrasts with zirconate, titanate, and hafnate pyrochlore compounds, which transform to the cotunnite-like structure at different pressures correlated with the cation radius ratio, r_A/r_B [3–15]. Because XRD data for the cotunnite-like phase could not be refined using the methods detailed here, the extent of the transition from pyrochlore to the high-pressure cotunnite-like phase was measured as a function of pressure using relative peak intensities (figure 4) [14]. Several previous studies on pyrochlore zirconates, titanates, and hafnates at high pressure have also used this method to qualitatively determine the extent of the phase transition versus pressure [4, 14, 15]. By 50 GPa, a lower percentage of $Er_2Sn_2O_7$ has transformed to the cotunnite-like phase than $Gd_2Sn_2O_7$. $Nd_2Sn_2O_7$ reaches a maximum cotunnite-like phase fraction at ~42 GPa, and does not progress further, even to 52 GPa. A sigmoidal trend is observed for $Nd_2Sn_2O_7$ and $Gd_2Sn_2O_7$, both of which exhibit an initial period of relatively sluggish transformation as a function of pressure below 35 GPa, and then rapidly progress through their transitions between 35 and 45 GPa ($Nd_2Sn_2O_7$) or 43–50 GPa ($Gd_2Sn_2O_7$). The transformation in $Er_2Sn_2O_7$ proceeds in a relatively linear fashion, as a function of pressure, as compared with $Nd_2Sn_2O_7$ and $Gd_2Sn_2O_7$.

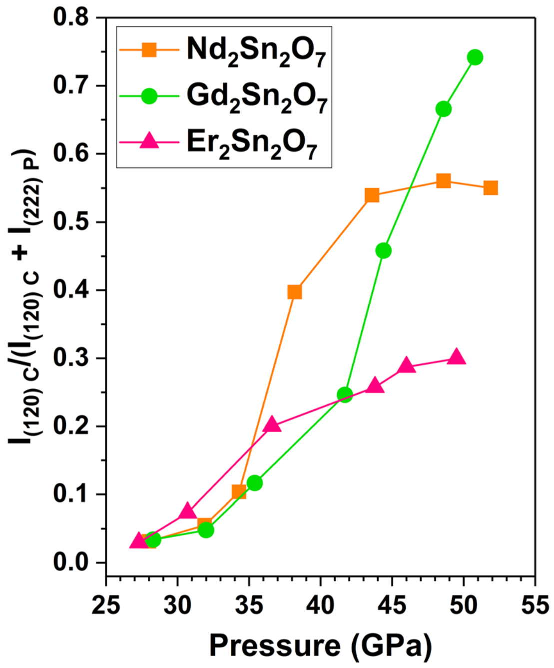

Figure 4. Normalized relative intensity of the strongest cotunnite-like structure peak (this is the (1 2 0) in an ideal cotunnite structure) to the (2 2 2) pyrochlore peak versus pressure in $Ln_2Sn_2O_7$ materials. These are the two strongest features for each phase and qualitatively indicate the extent of the pyrochlore-to-cotunnite-like phase transition versus pressure.

The bulk modulus, B_0, of these stannates increases with decreasing radius ratio, with a nearly linear slope (figure 5(b)). Similar inverse proportionality between the bulk moduli and cation radius ratios of the lanthanide hafnates have been

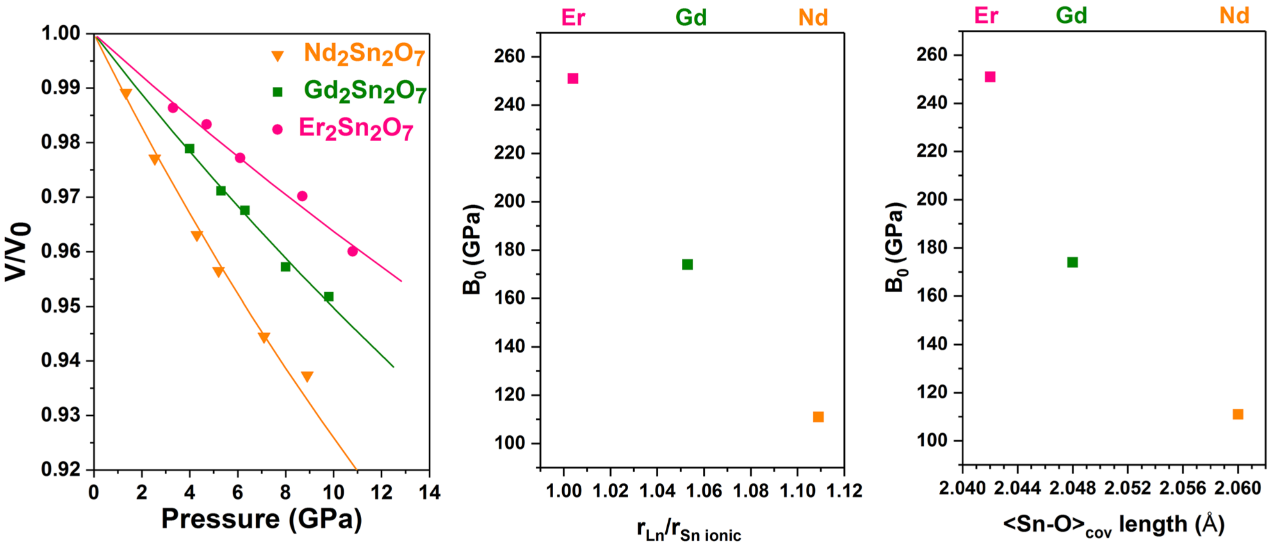

(a) (b) (c)

Figure 5. (a) P–V data (points) for lanthanide stannates, and 2nd-order Birch–Murnaghan equation of state fits for each composition (lines). (b) Bulk modulus, B_0, versus cation radius ratio of lanthanide stannates, (c) bulk modulus, B_0, versus ⟨Sn–O⟩ covalent bond length [58].

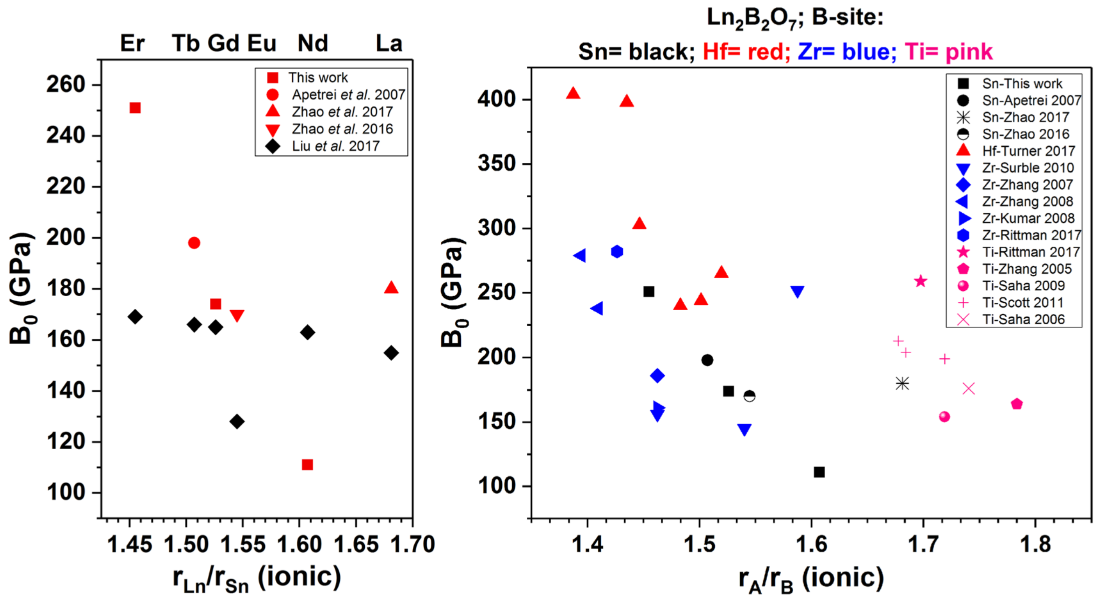

(a) (b)

Figure 6. (a) Compressibility of stannates from experimental studies and computational models (b) the experimentally-determined compressibility of stannate, hafnate, zirconate, and titanate pyrochlores versus ionic radius ratio from several studies.

reported, yet this relationship was not linear with respect to radius ratio [14]. Rather, the bulk modulus of hafnates reflected an inverse correlation with radius ratio, and a discontinuity was observed at r_A/r_B of 1.45, where the hafnates adopted a defect-fluorite structure versus a pyrochlore structure [14]. The linear trend of B_0 in stannates may reflect only a change in radius ratio, since all stannates adopt the pyrochlore structure. Inverse trends of bulk modulus with radius ratio have also been reported in pyrochlore zirconates. The bulk modulus, B_0, of these stannates is inversely proportional to the ⟨Sn–O⟩ bond lengths as calculated by Liu *et al* (figure 5(c)), however, this trend is nonlinear [20].

The P–V data up to ~12.5 GPa were fitted to 2nd Order Birch–Murnaghan equations of state (figure 5(a)). Only pressures below 12.5 GPa were used in the calculation of the bulk moduli, as this is near the hydrostatic limit for the pressure medium used, methanol and ethanol in a 4:1 ratio [41, 42]. At pressures beyond ~12.5 GPa, the samples may experience deviatoric stress [41, 42]; bulk modulus (B_0) is a parameter that assumes a hydrostatic stress state, therefore, higher pressure points were not used to fit B_0.

The bulk moduli from several experiments [3, 17, 18] on stannate pyrochlore are compared to the recent computational models of B_0 in stannates by Liu *et al* (figure 6(a)) [20]. The

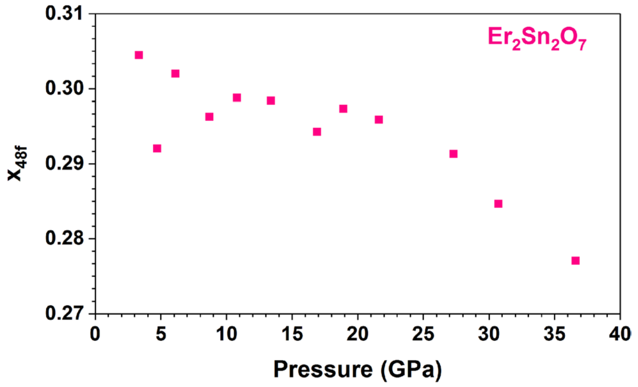

Figure 7. The response of the x_{48f} oxygen positional parameter to pressure in $Er_2Sn_2O_7$. Errors are smaller than the data points.

experimentally determined B_0 data for Er, Tb, Gd, Eu, and Nd stannates vary linearly and inversely with ionic radius ratio of Ln^{3+}/Sn^{4+}; the slope is −9.0733 GPa per .01 difference in the ionic radius ratio of Ln^{3+}/Sn^{4+}. A recent experimental study on $La_2Sn_2O_7$ found a B_0, 180 GPa, that is higher than expected for this trend [18]. The computational results from Liu *et al* also show an inverse trend with radius ratio, however the variation from $Er_2Sn_2O_7$ to $La_2Sn_2O_7$ is only 10 GPa (versus 140 GPa based on the various experimental results) [20].

The experimentally determined bulk moduli of pyrochlore titanates, zirconates, hafnates, and stannates from several studies versus ionic radius ratio are compared [3–18] in figure 6(b). Generally, pyrochlore stannates and zirconates show a linear relationship of bulk modulus versus cation radius ratio. The bulk moduli of pyrochlore zirconates, hafnates, and stannates show slopes of −10.154, −13.437, and −9.0733 GPa per 0.01 change in r_{Ln}/r_B, respectively. In contrast, the bulk moduli of the pyrochlore titanates vary with a slope of approximately −4.5608 GPa per 0.01 change in r_{Ln}/r_{Ti}.

The variation in the x_{48f} parameter versus pressure was refined for $Er_2Sn_2O_7$ (figure 7); the errors were too large for accurate refinement of this parameter in $Nd_2Sn_2O_7$ and $Gd_2Sn_2O_7$. The x_{48f} parameter decreases with pressure from ambient pressure to 40 GPa. Below 25 GPa, the change in the parameter is ~0.01; at pressures higher than 25 GPa, consistent with the onset of the phase transition, the x_{48f} parameter decreases more sharply by ~0.02 over a span of 15 GPa. The decrease in the 48*f* parameter is likely due to a shortening of the cation-oxygen bond lengths, as well as increasing disorder from cation anti-site defects and anion Frenkel pairs [21–24]. The 48*f* oxygen, in a perfect pyrochlore, is coordinated by two A-cations and two B-cations [1, 2]; as the pyrochlore disorders upon compression, the formation of defects and the compression of the structure causes a decrease in the 48*f* parameter. The further decrease in the 48*f* parameter after the onset of the phase transition to the cotunnite-like structure indicates that the coexisting pyrochlore phase is able to compress more easily above ~25 GPa; this could be due to an intrinsic property of pyrochlore, which would be reflected in a bulk modulus measurement of pyrochlore at these pressures or to deviatoric stress on the material from the non-hydrostatic environment [41, 42].

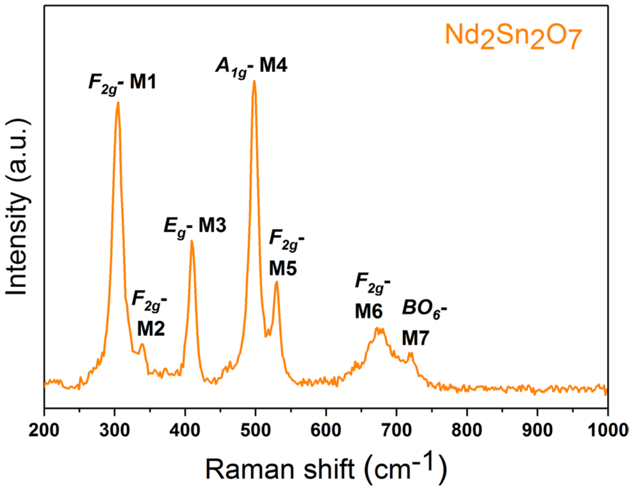

Figure 8. Raman spectrum of $Nd_2Sn_2O_7$ pyrochlore at ambient pressure, with labeled theoretical Raman-active modes: $4F_{2g} + E_g + A_{1g}$, and additional mode from BO_6 octahedral distortion.

Table 2. Frequencies (cm^{-1}) of Raman-active modes in $Ln_2Sn_2O_7$ pyrochlore in ambient conditions.

Composition	F_{2g} (M1)	F_{2g} (M2)	E_g (M3)	A_{1g} (M4)	F_{2g} (M5)	BO_6 (M7)
$Nd_2Sn_2O_7$	303	339	409	497	529	720
$Gd_2Sn_2O_7$	310	348	415	502	535	741
$Er_2Sn_2O_7$	308	355	412	505	535	751

In situ Raman spectroscopy

Raman spectroscopy provides information that is complementary to XRD data because it is more sensitive to changes on the anion sublattice than XRD, and it can elucidate changes to the local structure of pyrochlore [33]. Disordered $A_2B_2O_7$ materials possess at least two distinct length scales of structure: the long-range, periodic scale (cubic), and the local scale less than 10 Å (orthorhombic) [25, 27]. The short-range structure of the material has been shown in irradiated and compositionally disordered $A_2B_2O_7$ compounds to be an orthorhombic weberite-type, which is only evident in neutron diffraction pair-distribution function analysis [27] or by Raman spectroscopy [25]. The short-range weberite-type structure is unable to be resolved with conventional synchrotron XRD because it co-exists with the long-range average 'defect-fluorite' structure [27]; therefore unit cell parameters for the weberite-type structure are not presented.

The stannate pyrochlore compositions in this study each show Raman spectra typical of pyrochlore-structured oxides at ambient conditions (figure 8) [33]. Group theory analysis of the pyrochlore structure predicts six Raman active modes corresponding to vibrations of the ⟨A–O⟩ and ⟨B–O⟩ bonds [33]:

$$\Gamma^{\mathbf{crys}}_{\mathbf{Raman}} = A_{1g} + E_g + 4F_{2g}. \tag{1}$$

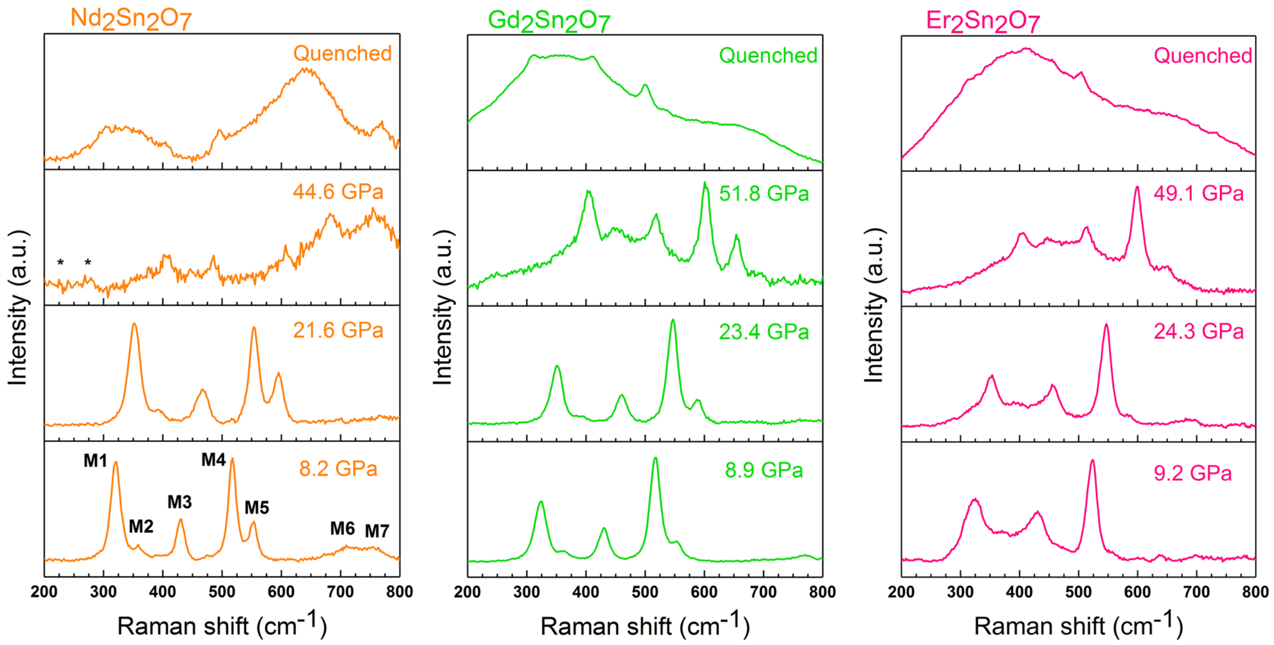

Figure 9. *In situ* Raman spectra of Nd-, Gd-, and Er- stannate pyrochlore at selected pressures up to 50 GPa and quenched to ambient pressure. Peaks indicated by asterisks in $Nd_2Sn_2O_7$ at 44.6 GPa are assigned to vibrations from the cotunnite-like high-pressure phase.

Additionally, an extra mode is often evident in the Raman spectra of pyrochlore-oxides between 700–800 cm^{-1}. This mode is attributed to the 'breathing' vibration of the BO_6 octahedra, and its presence indicates distortion from the ideal pyrochlore structure and coordination polyhedra [14, 33]. In an idealized pyrochlore structure, the B-site cations are coordinated by six anions in a distorted octahedron. Specifically, the B-site cations are coordinated by the 48*f* oxygens, and the vacant 8*b* site is tetrahedrally coordinated by B-cations [1]. The appearance of the BO_6 'breathing' mode in stannates as well as other pyrochlore oxides—notably hafnates, titanates, and zirconates [3–15], reflects a deviation from the ideal pyrochlore 48*f* positional parameter ($x_{48f} = 0.3125$) and partial occupancy of the normally empty 8*b* site [1].

The Raman spectra of rare-earth stannate pyrochlore compositions at ambient pressure show sharper and more well-defined peaks than hafnates [14] and zirconates [4, 15]; this may be due to the increased ionic radius ratio of stannates relative to hafnates and zirconates. The frequencies of the pyrochlore Raman-active modes M1–M5 and the BO_6 'breathing' mode at ambient pressure are shown in table 2. An accurate peak fitting for M6 could not be obtained. These positions are in good agreement with previous vibrational studies on rare-earth stannates [33].

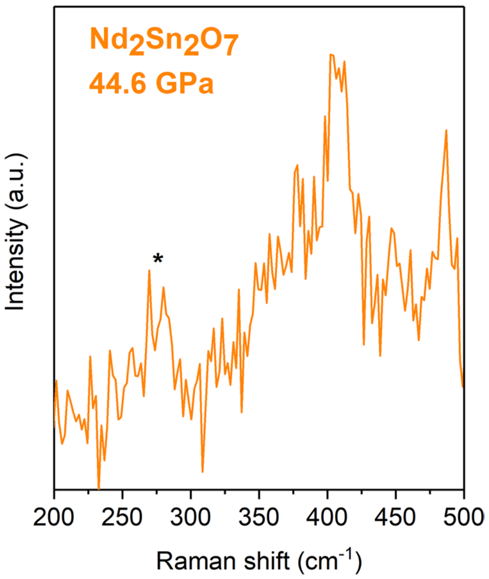

Figure 10. *In situ* Raman spectrum of $Nd_2Sn_2O_7$ at 44.6 GPa, showing new features (denoted by asterisk) likely from the high-pressure cotunnite-like phase.

Clear differences are observed in the Raman spectra of the different stannate pyrochlores under compression (figure 9). In $Nd_2Sn_2O_7$, the strongest peak at low pressures is the F_{2g} mode, M1. However, for $Gd_2Sn_2O_7$ and $Er_2Sn_2O_7$, the most intense vibration is the A_{1g} mode, M4. Additionally, $Nd_2Sn_2O_7$ shows a stronger contribution from the BO_6 breathing mode at 8.2 GPa relative to $Gd_2Sn_2O_7$ and $Er_2Sn_2O_7$ at similar pressures. Finally, the peaks are poorly resolved in $Er_2Sn_2O_7$ at 9.2 GPa, relative to $Gd_2Sn_2O_7$ and $Nd_2Sn_2O_7$. $Nd_2Sn_2O_7$ still shows each mode as a well separated peak. $Gd_2Sn_2O_7$ shows broad M1, M3, and M4 peaks, with M2 and M5 appearing as broad weak shoulders. $Er_2Sn_2O_7$ shows clearly evident, but relatively broad, M1, M3, and M4 modes, but the M2 and M5 modes are convoluted. Overall, the Raman spectra of the stannates show increasing broadening, and therefore likely increasing disorder and defect concentrations, as the cation radius ratio decreases.

At pressures above where the transformation to the cotunnite-like phase begins, the spectra of these three compounds clearly differ. In $Nd_2Sn_2O_7$, new features between 200–300 cm^{-1} are apparent (figure 10), which can possibly be attributed to the high-pressure cotunnite-like phase [4,

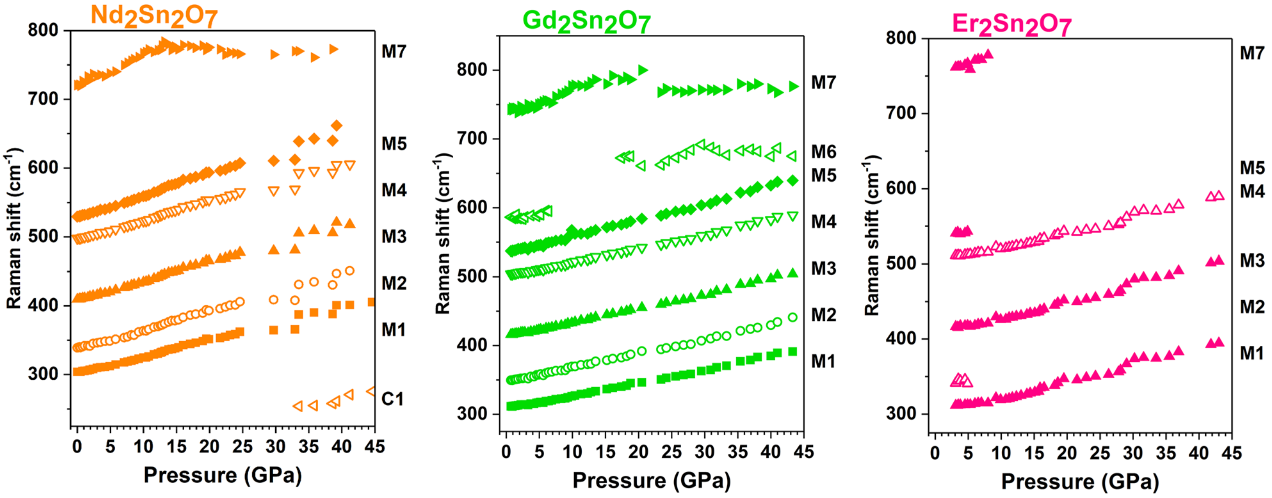

Figure 11. Peak positions of pyrochlore Raman-active modes (and mode from cotunnite-like phase in $Nd_2Sn_2O_7$) versus pressure in lanthanide stannates.

15]. The pyrochlore M1, M3, and M4 modes are still evident, but at reduced intensities. The highest-intensity feature in the spectra for $Nd_2Sn_2O_7$ is a broad band between 700 and 800 cm^{-1}. These peaks may be a combination of the M5, M6, and BO_6 modes in pyrochlore, broadened due to pressure-induced stress and disordering. The high intensity of this band, relative to the other modes, suggests that substantial distortion of the BO_6 octahedra occurs in the high-pressure phase. This contrasts with the spectra of $Gd_2Sn_2O_7$ and $Er_2Sn_2O_7$, for which no features are evident between 700 and 800 cm^{-1}. Modes in the 200–300 cm^{-1} region are not apparent for $Gd_2Sn_2O_7$ or $Er_2Sn_2O_7$. However, the XRD data for $Gd_2Sn_2O_7$ and $Er_2Sn_2O_7$ clearly show a transition to the cotunnite-like phase; the absence of new modes in the Raman spectra may mean that the high-pressure phase of these two compounds is particularly disordered. For $Gd_2Sn_2O_7$, the M4 A_{1g} mode is still the strongest mode at 51.8 GPa, but the other pyrochlore Raman-active modes are clearly present as well, indicating that the high-pressure local structure still partially retains pyrochlore-type ordering. This is consistent with the XRD data indicating that at the maximum pressure achieved and following decompression, $Gd_2Sn_2O_7$ still exhibited a pyrochlore-structured phase, in addition to the cotunnite-like phase. In $Er_2Sn_2O_7$ at high pressure, the pyrochlore Raman-active modes are still present at 49.1 GPa, but the peaks have significant overlap and the M5 mode is significantly diminished relative to $Gd_2Sn_2O_7$. The character of spectra from $Er_2Sn_2O_7$ and $Gd_2Sn_2O_7$ at ~50 GPa indicate the presence of pyrochlore-type order at the local level.

Spectra of these materials following decompression from ~50 GPa show two broad features: one centered at ~350 cm^{-1}, and one centered at ~680 cm^{-1}. Additionally, the M4 pyrochlore mode, the most intense mode at ambient conditions, is still apparent in each spectrum, although it is weak relative to the broad bands. However, the relative intensities of the two broad features differ between the compositions. In $Nd_2Sn_2O_7$, the feature at ~680 cm^{-1} is much more intense than that at ~350 cm^{-1}. In pyrochlore-structured oxides, this feature corresponds to stretching and bending of the ⟨B–O⟩ and ⟨O–B–O⟩ bonds, and the BO_6 breathing mode. However, spectra of this type have been observed in irradiated stannate pyrochlore [25] and pressure-treated hafnate pyrochlore [14] and indicate a weberite-type local structure [49–51]. When considered with the quenched XRD pattern of $Nd_2Sn_2O_7$ (figure 3), which shows a defect-fluorite average structure, it is likely that $Nd_2Sn_2O_7$ adopts the multi-scale structure of defect-fluorite and weberite-type seen in irradiated and compositionally-doped pyrochlore [25, 27].

The post-decompression spectra of $Gd_2Sn_2O_7$ and $Er_2Sn_2O_7$ show a stronger contribution from the lower frequency features, relative to $Nd_2Sn_2O_7$. In $Gd_2Sn_2O_7$, it is possible to distinguish individual peaks within the feature. Spectra of this type have been reported in $Sm_2Hf_2O_7$ pyrochlore compressed to 50 GPa and decompressed to ambient pressure, and were attributed to a defect-rich pyrochlore structure at the local level [14].

In $Nd_2Sn_2O_7$, M1, M2, M3, M4, and M5 increase nearly linearly with pressure between 0–45 GPa, with no discontinuities or changes in slope, even beyond the hydrostatic limit of the pressure medium (figure 11). M7, the BO_6 'breathing' mode shows similar behavior, but its frequency does not increase as abruptly after 15 GPa. This is likely not an artifact of the non-hydrostatic conditions in the sample chamber at 15 GPa [41, 42], because only M7 shows a slower rate of increase. Additionally, a similar change is not seen in $Gd_2Sn_2O_7$ or $Er_2Sn_2O_7$. However, similar behavior of the 'breathing' mode has been observed in the Raman spectra of lanthanide hafnate pyrochlores at high pressure [14]. The M7 mode corresponds to vibrations around the BO_6 octahedra; the change may be due to distortion of the octahedra reaching a near maximum around ~15 GPa, or due to defect formation. Anti-site cation defects would cause some octahedra to be AO_6, and Frenkel pairs would cause some of the polyhedral to increase in coordination number. In $Nd_2Sn_2O_7$, and in the previously reported hafnates [14], the change in the M7 mode slope may be due to a critical accumulation of the aforementioned defects in the structure causing a shift around the BO_6 octahedra that does not yet affect the long-term average structure (which is

Table 3. Mode Grüneisen parameters, $\gamma_{i0,}$ for Raman-active modes in lanthanide stannate pyrochore.

Mode	$Nd_2Sn_2O_7$	$Gd_2Sn_2O_7$	$Er_2Sn_2O_7$
M1	0.51	2.01	1.22
M2	0.83	1.87	2.58
M3	0.52	1.47	1.53
M4	0.39	2.70	2.01
M5	0.49	2.87	1.84
M7	0.51	1.40	3.52

why a phase transition is not seen in XRD data at these pressures). Pyrochlores with larger cation radius ratios tend to have higher defect-formation energies than ones with smaller cation radius ratios [21–24], which may be why this effect is seen in $Nd_2Sn_2O_7$ and previously in $Sm_2Hf_2O_7$ [14], but not stannates and hafnates with smaller lanthanides. The Raman spectra of $Er_2Sn_2O_7$ broaden and degrade at moderate pressures. Above 5 GPa only the strongest modes—the M1, M3, and M4—could be accurately resolved, and they were fit to 45 GPa. These three modes increase linearly with pressure with no discontinuities, as in the other compositions. Overall the frequency shifts as a function of pressure are similar in $Nd_2Sn_2O_7$ and $Gd_2Sn_2O_7$ even though the intensities of the peaks differ widely (figure 9). This suggests that similar processes take place at the local level, particularly involving the ⟨B–O⟩ bonds.

The mode Grüneisen parameter, γ_{io} [44], was calculated for each of the Raman-active modes in the compounds studied here (table 3); this parameter is a measure of compressibility on a local atomic level. The mode Grüneisen parameter is defined as:

$$\gamma_{i0} = B_0/\nu_{i0} * (\delta\nu_{i0}/\delta P)_0. \tag{2}$$

The average mode Grüneisen parameter increases with decreasing radius ratio. This is due in part to the increase in bulk modulus with the substitution of lanthanides of higher atomic number, but the average change in slope, $(\delta\nu_{i0}/\delta P)_0$ also increases with decreasing radius ratio. This indicates that as the cation radius ratio decreases, and the cations become more similar in size, the Raman modes become more sensitive to compression. Raman-active modes in pyrochlore materials correspond to vibrations of the ⟨A–O⟩ and ⟨B–O⟩ bonds, indicating that as r_A/r_B approaches 1, these bonds are more easily compressed and bent.

The relative FWHM of the low-frequency F_{2g} mode, M1, was measured as a function of pressure and is plotted for each composition (figure 12). The FWHM of this peak is a qualitative proxy for the extent of disordering on the cation and anion sublattices in pyrochlore-structured materials [14]. Raman spectroscopy is more sensitive to changes in the oxygen sublattice than XRD, due to the weak scattering of x-rays by relatively light oxygen. However, because changes to the cation sublattice will affect the vibrational environment around oxygen anions, cation- and anion-specific disordering can be decoupled only to a limited extent. Still, distinct compositional trends can be seen. All of the materials studied exhibit immediate increases in FWHM with pressure, indicating that disordering begins at the onset of compression. Previous studies of pyrochlore compounds have postulated that this initial disorder is due primarily to atomic displacement on the anion-sublattice [15]. The rate of broadening of the FWHM is lowest in $Nd_2Sn_2O_7$, and increases with decreasing cation radius ratio. This indicates that disorder proceeds more easily for stannate compositions with similarly-sized cations. This is consistent with results showing that the defect-formation energy for cation anti-site defects and anion Frenkel pairs in pyrochlore oxides is smaller for materials with a lower cation radius ratio [21–24]. Similar results have been seen in hafnate pyrochlores [14].

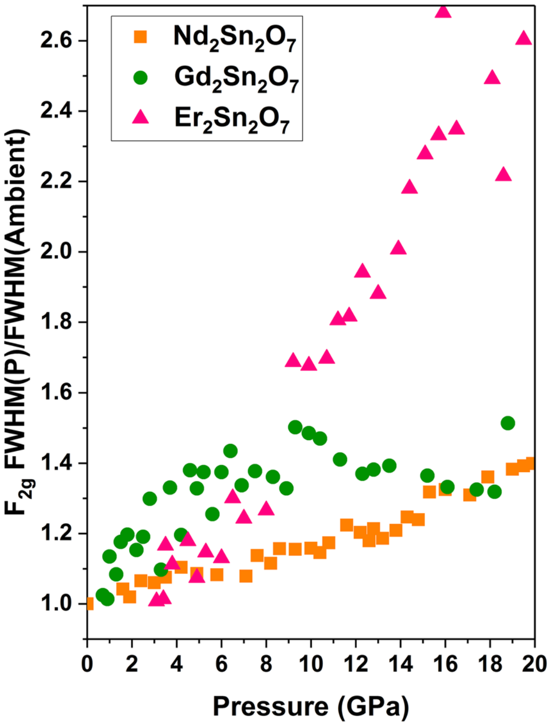

Figure 12. Relative FWHM of F_{2g} (M1) Raman active mode versus pressure in lanthanide stannate pyrochlore. Relative FWHM of the F_{2g} mode is a qualitative proxy for anion and cation sublattice disordering in pyrochlore.

Discussion

While the stannate pyrochlores studied here show some similarities to the pyrochlore hafnates, zirconates, and titanates [3–15], there are notable differences. *In situ* synchrotron XRD data indicated that rare-earth stannates begin to transform to a cotunnite-like structure at ~28 GPa. This pressure-induced transformation has been previously seen in lanthanide zirconates, hafnates, and titanates with pyrochlore and defect-fluorite type structures under high pressure [3–15]. In hafnates, the phase transition to the cotunnite-like phase begins at less than 25 GPa [14]. In zirconates, the phase transition can begin as low as 16 GPa, and in titanates as high as 40 GPa [15]. The phase transition progresses furthest in stannates with larger lanthanides: $Gd_2Sn_2O_7$ and $Nd_2Sn_2O_7$. The phase transition extent versus pressure contrasts with the behavior of rare-earth hafnates, zirconates, and titanates, which show a further extent of phase transition in materials with smaller lanthanides [14]. Additionally, pyrochlore titanates and zirconates with a higher initial extent of disorder showed a further progression of the pressure-induced phase transition than those with less disorder [15]. This may be due to the extent of cation disorder: pyrochlore compositions with lower radius ratio are generally more susceptible to inherent cation-sublattice disorder [29–31], which may hinder the pressure-induced phase transition. However, in stannates, the difference in disordering energy per formula unit is <0.5 eV between $Er_2Sn_2O_7$ ($r_A/r_B = 1.46$) and $Nd_2Sn_2O_7$ ($r_A/r_B = 1.61$) [55]. In comparable zirconates, the difference in disordering energy is >1 eV [55]. Therefore, differences in cation radius ratio may not play as large a role in compression-induced phase behavior in stannates versus zirconates, titanates, and hafnates. This trend in disordering energy could explain the identical phase transition onset pressure in stannates of 28 GPa, regardless of Ln^{3+} size. In a computational study on $Y_2B_2O_7$ pyrochlore with either Zr^{4+}, Ti^{4+}, or Sn^{4+} as the B-site cation, $Y_2Sn_2O_7$ had the highest anti-site defect formation energy, even though it has an intermediate cation radius ratio as compared with the other compositions [55]. This high defect formation energy was due to the greater covalency of the ⟨Sn–O⟩ bond [55]. The ⟨Sn–O⟩ bond covalency may have a greater influence on compression-induced structural behavior in pyrochlore stannates with smaller Ln^{3+} size, since the energetics of defect formation in stannates are more constant across the lanthanide series than for zirconates, titanates, and hafnates [55].

The compressibility of pyrochlore stannates increases with decreasing Ln^{3+} ionic radius, a trend that is consistent with the observed behavior of pyrochlore hafnates, zirconates, and titanates [3–15]. Additionally, the range of values: 111–251 GPa, compares well with pyrochlore titanates, zirconates, and hafnates [3–15]. The slopes of B_0 versus r_A/r_B are more similar between zirconates, hafnates, and stannates, than titanates (figure 6(b)). In previous computational studies of pyrochlores, the bulk modulus is thought to relate strongly to the size of the Ln^{3+} cation, rather than the B^{4+} cation [19]. From this work (figure 6(b)), it is evident that for a single B-site composition—titanate, zirconate, hafnate, or stannate—the size of Ln^{3+} affects the bulk modulus. Additionally, the zirconates, hafnates, and stannates show similar trends when compared versus r_A/r_B. However, the pyrochlore titanates have systematically higher B_0 versus r_A/r_B than would be expected for either of the zirconates, hafnates, and stannates. The pyrochlore titanates are some of the most ionic of the ones compared in figure 6(b), and additionally they have some of the largest cation radius ratios ($r_A/r_{Ti} > 1.6$).

Recent experimental work on $La_2Sn_2O_7$ at high pressure showed an anomalously high B_0, 180 GPa, when compared with other experiments on $Eu_2Sn_2O_7$, $Nd_2Sn_2O_7$, $Gd_2Sn_2O_7$, and $Er_2Sn_2O_7$ [3, 16–18]. However, the $La_2Sn_2O_7$ pyrochlore behaved differently at high pressure than the aforementioned others; it began to decompose into a ternary oxide and metallic Sn at pressures of ~13 GPa. $La_2Sn_2O_7$ did not show a phase transition to the cotunnite-like phase at high pressure. It is possible that in addition to Ln^{3+} size, the type of structural phase transitions undergone by pyrochlore oxides at high pressure influences the compressibility.

A recent computational study of stannate pyrochlore at high pressure modeled the compressibility across the lanthanide series [19] (figure 6(a)). The authors predicted B_0 to vary between ~160–170 GPa between $La_2Sn_2O_7$ and $Er_2Sn_2O_7$, with the exception of $Eu_2Sn_2O_7$, which is predicted to have a much lower B_0 of 130 GPa. In comparing the compressibilities in the recent computational study to the ones found in this study, as well as three other experimental studies [16–18], there is a much more dramatic variation in B_0 across the lanthanide series. The values reported from experiments [16–18] vary between ~110–250 GPa (figure 6(a)). The values predicted computationally for $Tb_2Sn_2O_7$ and $Gd_2Sn_2O_7$ are close to experimentally recorded values, but for the other lanthanides, the discrepancy is larger than 20 GPa.

In addition to compressibility, the recent computational study by Liu *et al* predicted that the x_{48f} parameter in stannate pyrochlore would increase as a result of hydrostatic compression [19]. The present work shows that for $Er_2Sn_2O_7$ the x_{48f} parameter decreased, rather than increased by 0.06 as predicted by Liu *et al*, upon compression. A decreasing x_{48f} parameter versus pressure has also been observed experimentally in $Eu_2Sn_2O_7$ pyrochlore [17]. The 48*f* parameter is an indicator of polyhedral distortion in pyrochlore compounds; a smaller 48*f* parameter reflects compression-induced distortion of the AO_8 and BO_6 polyhedra (figure 1(b)).

When stannates were decompressed from 50 GPa to ambient pressure, XRD patterns indicated a relaxation to the pyrochlore structure in $Gd_2Sn_2O_7$ and $Er_2Sn_2O_7$ as evidenced by the persistence of the (1 1 1) supercell diffraction maxima, as compared with the defect-fluorite diffraction maxima. This has not been observed previously in compressed pyrochlore oxides of the hafnate, zirconate, or titanate compositions, and may be unique to the stannates. A recent study on $Eu_2Sn_2O_7$ at high pressure also found that the material reverted to a pyrochlore structure after decompression [19]. $Nd_2Sn_2O_7$ adopted a defect-fluorite average structure after release of pressure (figure 3), which is typical of pyrochlore zirconates and hafnates [14].

The Raman spectroscopy of stannate pyrochlore compositions at high pressure showed mostly pyrochlore-Raman active modes, except in $Nd_2Sn_2O_7$, where high frequency modes between 700–800 cm^{-1} were dominant in the spectra above 40 GPa. The behavior of $Nd_2Sn_2O_7$ is typical of pyrochlore zirconates, titanates, and hafnates at high pressure [3–15]. However, the behavior of $Gd_2Sn_2O_7$ and $Er_2Sn_2O_7$ is unusual when compared with zirconates, titanates, and hafnates at high pressure [3–15]. When decompressed, all compositions still had the M4 mode typical of pyrochlore-structured oxides. Gd- and Er- stannate showed Raman spectra indicating a defect-rich pyrochlore, also seen previously in $Sm_2Hf_2O_7$. $Nd_2Sn_2O_7$ showed spectra more typical of defect-fluorite or weberite-type structures seen previously in irradiated stannate pyrochlore and compressed hafnate and zirconate pyrochlore.

The structural response of stannate pyrochlore to extreme environments such as ion irradiation has recently been of interest [25]. The cation radius ratio, r_A/r_B, has been shown and proposed to be the governing parameter in the tendency of a pyrochlore to amorphize or disorder under ion irradiation. Pyrochlores with smaller B-cations-e.g. titanates-tend to amorphize under ion irradiation, and pyrochlores with larger B-cations-e.g. zirconates-tend to disorder. However, until recently, this principle had been demonstrated primarily on pyrochlore zirconates and titanates [25]. Others have proposed that bond covalency would also determine whether a pyrochlore would disorder or amorphize under ion irradiation [25]. Recent work on stannates under ion irradiation found that these materials are significantly more resistant to amorphization than lanthanide titanates, even though the $\langle \text{Sn–O} \rangle$ bond is more covalent than the $\langle \text{Ti–O} \rangle$ bond [25]. Therefore, the response was consistent with cation radius ratio being the governing parameter determining response to irradiation even in a more covalently bonded pyrochlore.

Conclusions

The structural response of the pyrochlore structure to high pressure and ion irradiation is governed by the same factors. Pyrochlores that are more likely to amorphize as a result of compression and decompression should also amorphize under ion irradiation. The behavior of the stannates at high pressure demonstrates this principle. Overall, stannates show similar behavior to titanates, zirconates, and hafnates under high pressure: (1) the transition to the cotunnite-like high pressure phase (at ~28 GPa in stannates), (2) the inverse relation between compressibility and r_A/r_B, (3) the onset of local disordering on the anion sublattice at pressures as low as ~0.3 GPa. The Sn^{4+} cation is close in size (0.69 Å) to Zr^{4+} (0.71 Å) and Hf^{4+} (0.72 Å); Ti^{4+} is considerably smaller (0.61 Å). The trends in B_0 amongst these four families of pyrochlore (figure 6(b)) show the effect of cation size—both A cation and B cation—dominates the compressibility. The compressibility of stannates, zirconates, and hafnates are more similar to each other than to the compressibility of titanates.

Under compression, stannates are resistant to amorphization, like the zirconates and hafnates; they transform to either an ordered pyrochlore structure or the disordered multiscale defect-fluorite+ weberite-type structure upon compression to 50 GPa and subsequent decompression. Stannate pyrochlores under irradiation were also resistant to amorphization, and tended to transform to the disordered multiscale defect-fluorite+ weberite-type structure This behavior overall is consistent with cation radius ratio being the dominant property that influences compression response, even in a covalently bonded pyrochlore. Furthermore, this is consistent with the observation that the structural response of pyrochlore materials to ion-irradiation and compression are governed by the same properties.

Acknowledgments

This work was supported as part of the Materials Science of Actinides, an Energy Frontier Research Center funded by the US Department of Energy, Office of Science, Basic Energy Science under Award no. DE-SC0001089. Portions of this work were performed at the Beamline 12.2.2 of the ALS, Lawrence Berkeley National Laboratory. The ALS is a DOE Office of Science User Facility under contract no. DE-AC02-05CH11231. KMT gratefully acknowledges the Stanford University Diversifying Academia Recruiting Excellence (DARE) fellowship for graduate student funding. Finally, the authors thank beamline scientist Dr Christine Beavers (ALS) for her invaluable help setting up the XRD experiments.

ORCID iDs

Katlyn M Turner https://orcid.org/0000-0002-0064-1364

References

[1] Subramanian M A, Aravamudan G and Subba Rao G V 1983 Oxide pyrochlores—a review *Prog. Solid State Chem.* **15** 55–143

[2] Chakoumakos B C 1984 Systematics of the pyrochlore structure type, ideal $A_2B_2X_6Y$ *J. Solid State Chem.* **53** 120–9

[3] Zhang F X, Lang M and Ewing R C 2016 Phase transition and water incorporation into $Eu_2Sn_2O_7$ pyrochlore at high pressure *Chem. Phys. Lett.* **650** 138

[4] Rittman D R, Turner K M, Park S, Fuentes A F, Yan J, Ewing R C and Mao W L 2017 High-pressure behavior of $A_2B_2O_7$ pyrochlore (A = Eu, Dy; B = Ti, Zr) *J. Appl. Phys.* **121** 045902

[5] Xiao H Y, Zhang F X, Gao F, Lang M, Ewing R C and Weber W J 2010 Zirconate pyrochlores under high pressure *Phys. Chem. Chem. Phys.* **12** 12472–7

[6] Zhang F X, Lian J, Becker U, Ewing R C, Hu J and Saxena S K 2007 High-pressure structural changes in the $Gd_2Zr_2O_7$ pyrochlore *Phys. Rev.* B **76** 214104

[7] Zhang F X, Lian J, Becker U, Wang L M, Hu J, Saxena S K and Ewing R C 2007 Structural distortions and phase transformations in $Sm_2Zr_2O_7$ pyrochlore at high pressures *Chem. Phys. Lett.* **441** 216–20

[8] Zhang F X, Wang J W, Lian J, Lang M K, Becker U and Ewing R C 2008 Phase stability and pressure dependence of defect formation in $Gd_2Ti_2O_7$ and $Gd_2Zr_2O_7$ pyrochlores *Phys. Rev. Lett.* **100** 045503

[9] Zhang F X, Lang M, Becker U, Ewing R C and Lian J 2008 High pressure phase transitions and compressibilities of $Er_2Zr_2O_7$ and $Ho_2Zr_2O_7$ *Appl. Phys. Lett.* **92** 011909

[10] Zhang F X, Lang M, Tracy C L, Ewing R C, Gregg D J and Lumpkin G R 2014 Incorporation of uranium in pyrochlore oxides and pressure-induced phase transitions *J. Solid State Chem.* **219** 49–54

[11] Zhang F X and Saxena S K 2005 Structural changes and pressure-induced amorphization in rare earth titanates $RE_2Ti_2O_7$ (RE: Gd, Sm) with pyrochlore structure *Chem. Phys. Lett.* **413** 248–51

[12] Zhang F X, Manoun B and Saxena S K 2006 Pressure-induced order—disorder transitions in pyrochlore: $Re_2Ti_2O_7$ (Re = Y, Gd) *Mater. Lett.* **60** 2773–6

[13] Zhang F X, Lang M, Liu Z and Ewing R C 2010 Pressure-induced disordering and anomalous lattice expansion in a $La_2Zr_2O_7$ pyrochlore *Phys. Rev. Lett.* **105** 015503

[14] Turner K M, Rittman D R, Heymach R A, Tracy C L, Turner M L, Fuentes A F, Mao W L and Ewing R C 2017 Pressure-induced structural modifications of rare earth hafnate pyrochlore *J. Phys.: Condens. Matter* **29** 255401

[15] Rittman D R, Turner K M, Fuentes A F, Park C, Mao W L and Ewing R C 2017 Strain engineered pyrochlore at high pressure *Sci. Rep.* **7** 2236

[16] Apetrei A, Mirebeau I, Goncharenko I and Chrichton W 2007 Crystal structure under pressure of geometrically frustrated pyrochlores *J. Phys.: Condens. Matter* **19** 376208

[17] Zhao Y, Yang W, Li N, Li Y, Tang R, Li H, Zhu H, Zhu P and Wang X 2016 Pressure-enhanced insulating state and trigonal distortion relaxation in geometrically frustrated pyrochlore $Eu_2Sn_2O_7$ *J. Phys. Chem.* **120** 9436–42

[18] Zhao Y, Li N, Xu C, Li Y, Zhu H, Wang P, Wang X and Yang W 2017 Abnormal pressure-induced photoluminescence enhancement and phase decomposition in pyrochlore $La_2Sn_2O_7$ *Adv. Mater.* **29** 1701513

[19] Garg N, Pandey K, Murli C, Shanavas K, Mandal B, Tyagi A and Sharma S 2008 Decomposition of lanthanum hafnate at high pressures *Phys. Rev.* B **77** 214105

[20] Liu C, Zhang J, Chen L, Wen J, Dong L, Yang D and Li Y 2017 The structural parameters, structural stability, and bulk modulus in $RE_2Sn_2O_7$ by first-principles calculations *Int. J. Mod. Phys.* B **31** 1750184

[21] Minervini L and Grimes R W 2000 Disorder in pyrochlore oxides *J. Am. Ceram. Soc.* **83** 1873–8

[22] Minervini L, Grimes R W, Tabira Y, Withers R L and Sickafus K E 2002 The oxygen positional parameter in pyrochlores and its dependence on disorder *Phil. Mag.* A **82** 123–35

[23] Pirzada M, Grimes R W, Minervini L, Maguire J F and Sickafus K E 2001 Oxygen migration in $A_2B_2O_7$ pyrochlores *Solid State Ion.* **140** 201–8

[24] Wilde P J and Catlow C R A 1998 Defects and diffusion in pyrochlore structured oxides *Solid State Ion.* **112** 173–83

[25] Tracy C L, Shamblin J, Park S, Zhang F, Trautmann C, Lang M and Ewing R C 2016 Role of composition, bond covalency, and short-range order in the disordering of stannate pyrochlores by swift heavy ion irradiation *Phys. Rev.* B **94** 064102

[26] Lang M, Zhang F, Zhang J, Wang J, Lian J, Weber W J, Schuster B, Trautmann C, Neumann R and Ewing R C 2010 Review of $A_2B_2O_7$ pyrochlore response to irradiation and pressure *Nucl. Instrum. Methods Phys. Res.* B **268** 2951–9

[27] Shamblin J, Feygenson M, Neuefeind J, Tracy C L, Zhang F, Finkeldei S, Bosbach D, Zhou H, Ewing R C and Lang M 2016 Probing disorder in isometric pyrochlore and related complex oxides *Nat. Mater.* **15** 507–11

[28] Ewing R C, Weber W J and Lian J 2004 Nuclear waste disposal—pyrochlore ($A_2B_2O_7$): nuclear waste form for the immobilization of plutonium and 'minor' actinides *J. Appl. Phys.* **95** 5949–71

[29] Maczka M, Sanjuan M L, Fuentes A F, Hermanowicz K and Hanuza J 2008 Temperature-dependent Raman study of the spin-liquid pyrochlore $Tb_2Ti_2O_7$ *Phys. Rev.* B **78** 134420

[30] Maczka M, Sanjuan M L, Fuentes A F, Macalik L, Hanuza J, Matsuhira K and Hiroi Z 2009 Temperature-dependent studies of the geometrically frustrated pyrochlores $Ho_2Ti_2O_7$ and $Dy_2Ti_2O_7$ *Phys. Rev.* B **79** 214437

[31] Sanjuan M L, Guglieri C, Diaz-Moreno S, Aquilanti G, Fuentes A F, Olivi L and Chaboy J 2011 Raman and x-ray absorption spectroscopy study of the phase evolution induced by mechanical milling and thermal treatments in $R_2Ti_2O_7$ pyrochlores *Phys. Rev.* B **84** 104207

[32] Brisse F and Knop O 1967 Pyrochlores. III. X-ray, neutron, infrared, and dielectric studies of $A_2Sn_2O_7$ stannates *Can. J. Chem.* **46** 859

[33] Vandenborre M, Husson E, Chatry J P and Michel D 1983 Rare-earth titanates and stannates of pyrochlore structure; vibrational spectra and force fields *J. Raman Spectrosc.* **14** 63

[34] Chen L, Su X and Li Y 2014 First-principles study on cation-antisite defects of stannate and titanate pyrochlores *Open Acc. Lib. J.* **1** 1

[35] Chen Z J, Xiao H Y, Zu X T, Wang L M, Gao F, Lian J and Ewing R C 2008 Structural and bonding properties of stannate pyrochlores: a density function theory investigation *Comput. Mater. Sci.* **42** 653

[36] Wuensch B, Eberman K, Heremans C, Ku E, Onnerud P, Yeo E, Haile S, Stalick J and Jorgenson J 2000 Connection between oxygen-ion conductivity of pyrochlore fuel-cell materials and structural change with composition and temperature *Solid State Ion.* **129** 111

[37] Bondah-Jagalu V and Bramwell S 2001 Magnetic susceptibility study of the heavy rare-earth stannate pyrochlores *Can. J. Phys.* **79** 1381

[38] Lian J, Ewing R C, Wang L M and Helean K B 2011 Ion-beam irradiation of $Gd_2Sn_2O_7$ and $Gd_2Hf_2O_7$ pyrochlore: bond-type effect *J. Mater. Res.* **19** 1575

[39] Lang M *et al* 2015 Characterization of ion-induced radiation effects in nuclear materials using synchrotron x-ray techniques *J. Mater. Res.* **30** 1366

[40] Mao H K, Bell P M, Shaner J W and Steinberg D J 1978 Specific volume measurements of Cu, Mo, Pd, and Ag and calibration of the ruby R1 fluorescence pressure gauge from 0.06 to 1 Mbar *J. Appl. Phys.* **49** 3276–83

[41] Piermarini G J, Block S and Barnett J D 1973 Hydrostatic limits in liquids and solids to 100 kbar *J. Appl. Phys.* **44** 5377–82

[42] Angel R, Bujak M, Zhao J, Gatta G D and Jacobsen S D 2007 Effective hydrostatic limits of pressure media for high-pressure crystallographic studies *J. Appl. Crystallogr.* **40** 26–32

[43] Wojdyr M 2010 Fityk: a general-purpose peak fitting program *J. Appl. Crystallogr.* **43.5** 1126–8

[44] Sherman W F 1982 Pressure-induced changes in mode Grüneisen parameters and general equations of state for solids *J. Phys. C: Solid State Phys.* **15** 9–23

[45] Prescher C and Prakapenka V B 2015 DIOPTAS: a program for reduction of two-dimensional x-ray diffraction data and data exploration *High Press. Res.* **35** 223–30

[46] Lutterotti L, Matthies S and Wenk H R 1999 MAUD: a friendly Java program for material analysis using diffraction *IUCr: Newsl. CPD* **21** 14–5

[47] Birch F 1947 Finite elastic strain of cubic crystals *Phys. Rev.* **71** 809

[48] Angel R, Alvaro M and Gonzalez-Platas J 2014 EosFit7c and a Fortran module (library) for equation of state calculations *Z. Kristallogr.* **229** 405–19

[49] Siqueira K, Soares J, Granado E, Bittar E, de Paula A, Moreira R and Dias A 2014 Synchrotron x-ray diffraction and Raman spectroscopy of Ln_3NbO_7 (Ln = La, Pr, Nd, Sm–Lu) ceramics obtained by molten-salt synthesis *J. Solid State Chem.* **209** 63–8

[50] Preux N, Rolle A, Merlin C, Benamira M, Malys M, Estournes C, Rubbens A and Vannier R 2010 La_3TaO_7

derivatives with weberite structure type: possible electrolytes for solid oxide fuel cells and high temperature electrolysers *C. R. Chim.* **13** 1351–8

[51] Siqueira K, Borges R, Granado E, Malard L, de Paula A, Moreira R, Bittar E and Dias A 2013 Crystal structure of fluorite-related Ln_3SbO_7 (Ln = La-Dy) ceramics studied by synchrotron x-ray diffraction and Raman scattering *J. Solid State Chem.* **203** 326–32

[52] Fuentes A, Boulahya K, Maczka M, Hanuza J and Amador U 2005 Synthesis of disordered pyrochlores, $A_2Ti_2O_7$ (A = Y, Gd, and Dy), by mechanical milling of constituent oxides *Solid State Sci.* **7** 343–53

[53] Moreno K, Fuentes A, Maczka M, Hanuza J and Amador U 2006 Structural manipulation of pyrochlores: thermal evolution of metastable $Gd_2(Ti_{1-y}Zr_y)_2O_7$ powders prepared by mechanical milling *J. Solid State Chem.* **179** 3805–13

[54] Hayun S, Tran T, Lian J, Fuentes A and Navrotsky A 2012 Energetics of stepwise disordering transformation in pyrochlores, $RE_2Ti_2O_7$ (RE = Y, Gd, and Dy) *Acta Mater.* **60** 4303–10

[55] Panero W, Stixrude L and Ewing R 2004 First-principles calculation of defect-formation energies in the $Y_2(Ti, Sn, Zr)_2O_7$ pyrochlore *Phys. Rev.* B **70** 054110

[56] Williford R, Weber W, Devanathan R and Gale J 1999 Effects of cation disorder on oxygen vacancy migration in $Gd_2Ti_2O_7$ *J. Electroceram.* **3** 409–24

[57] Jiang C, Stanek C, Sickafus K and Uberuaga B 2009 First-principles prediction of disordering tendencies in pyrochlore oxides *Phys. Rev.* B **79** 104203

[58] Kennedy B, Hunter B and Howard C 1997 Structural and bonding trends in tin pyrochlore oxides *J. Solid State Chem.* **130** 58

[59] Lian J, Helean K, Kennedy B, Wang L, Navrostky A and Ewing R 2006 Effect of structure and thermodynamic stability on the response of lanthanide stannate pyrochlores to ion beam irradiation *J. Phys. Chem.* B **110** 2343